Stabilization of Single Metal Atoms on Graphitic Carbon Nitride

Zupeng Chen, Sharon Mitchell, Evgeniya Vorobyeva, Rowan K. Leary, Roland Hauert, Tom Furnival, Quentin M. Ramasse, John M. Thomas, Paul A. Midgley, Dariya Dontsova, Markus Antonietti, Sergey Pogodin, Núria López, and Javier Pérez-Ramírez*

Graphitic carbon nitride (g-C$_3$N$_4$) exhibits unique properties as a support for single-atom heterogeneous catalysts (SAHCs). Understanding how the synthesis method, carrier properties, and metal identity impact the isolation of metal centers is essential to guide their design. This study compares the effectiveness of direct and postsynthetic routes to prepare SAHCs by incorporating palladium, silver, iridium, platinum, or gold in g-C$_3$N$_4$ of distinct morphology (bulk, mesoporous and exfoliated). The speciation (single atoms, dimers, clusters, or nanoparticles), distribution, and oxidation state of the supported metals are characterized by multiple techniques including extensive use of aberration-corrected electron microscopy. SAHCs are most readily attained via direct approaches applying copolymerizable metal precursors and employing high surface area carriers. In contrast, although post-synthetic routes enable improved control over the metal loading, nanoparticle formation is more prevalent. Comparison of the carrier morphologies also points toward the involvement of defects in stabilizing single atoms. The distinct metal dispersions are rationalized by density functional theory and kinetic Monte Carlo simulations, highlighting the interplay between the adsorption energetics and diffusion kinetics. Evaluation in the continuous three-phase semihydrogenation of 1-hexyne identifies controlling the metal–carrier interaction and exposing the metal sites at the surface layer as key challenges in designing efficient SAHCs.

1. Introduction

Single-atom heterogeneous catalysts (SAHCs) receive considerable attention aiming to combine the excellent metal utilization attained by homogeneous catalysts with the robustness and facile recovery offered by traditional heterogeneous catalysts.[1] During the past decade, the realization that single atoms could significantly contribute to the activity of heterogeneous catalysts has sparked huge debate over the extent of their role.[2] These contentions primarily arise due to the challenges associated with the effective stabilization of single atoms on a given carrier and with verifying the single-atom nature. The latter architecture has been obtained in isolated metals on inert metal matrices,[1b,3] metal oxides,[1c] and porous carbon materials.[4] Progress in this area has generated ample evidence to show that supported single Pt, Ir, and Pd atoms are active in the selective hydrogenation reactions of alkynes, nitroarenes, and alkenes.[1e,5]

Controlling the interaction of the metal species with the carrier is expected to be the key to stabilize single atoms,[6] preventing agglomeration due to the increasing cohesive energy upon forming metal species without diminishing the activity by changing the electronic configuration. Therefore, only a flexible carrier that sufficiently interacts with the isolated metal centers can circumvent this energy conundrum. Recently, single atoms of Pd were successfully isolated on mesoporous graphitic carbon nitride (g-C$_3$N$_4$),[5a,7] which converted 1-hexyne to 1-hexene with high rates and 99% selectivity. Subsequently, an Ag/g-C$_3$N$_4$

Dr. Z. Chen, Dr. S. Mitchell, E. Vorobyeva, Prof. J. Pérez-Ramírez
Institute for Chemical and Bioengineering
Department of Chemistry and Applied Biosciences
ETH Zürich
Vladimir-Prelog-Weg 1, 8093 Zürich, Switzerland
E-mail: jpr@chem.ethz.ch

Dr. R. K. Leary, T. Furnival, Prof. J. M. Thomas, Prof. P. A. Midgley
Department of Materials Science and Metallurgy
University of Cambridge
27 Charles Babbage Road, Cambridge CB3 0FS, UK

Dr. R. Hauert
EMPA
Swiss Federal Laboratories for Materials Science and Technology
Überlandstrasse 129, 8600 Dübendorf, Switzerland

Prof. Q. M. Ramasse
SuperSTEM Laboratory
SciTech Daresbury Campus
Keckwick Lane, Warrington WA4 4AD, UK

Dr. D. Dontsova, Prof. M. Antonietti
Department of Colloid Chemistry
Max Planck Institute of Colloids and Interfaces
14424 Potsdam, Germany

Dr. S. Pogodin, Prof. N. López
Institute of Chemical Research of Catalonia (ICIQ)
The Barcelona Institute of Science and Technology
Av. Països Catalans 16, 43007 Tarragona, Spain

SAHC also outperformed other state-of-the-art Ag-based materials in selective hydrogenations,[8] while a Pt/g-C₃N₄ SAHC exhibited remarkable photocatalytic activity.[9] Although these findings have clearly demonstrated the potential of g-C₃N₄ as a single-atom host, the method of metal introduction and the type and amount of metal incorporated differed in each case. Hence, it remains difficult to derive synthesis-property relations for the improved design of SAHCs.

Graphitic carbon nitride is the most stable allotrope of carbon nitride under ambient conditions.[10] Though the precise atomic structure is often debated, most experimental studies have concluded that the polycondensation of common precursors as cyanamide or dicyandiamide predominantly yields tri-s-triazine based structures,[11] which were also predicted to be more thermodynamically stable by Density Functional Theory (DFT).[12] The morphology of g-C₃N₄ can be readily manipulated to develop high surface area. For example, mesoporous g-C₃N₄ (MCN) can be obtained through the use of different templates, while the graphitic layers of bulk g-C₃N₄ (BCN) can be exfoliated into nanosheets (ECN) by thermal treatment. This aspect coupled with the presence of nitrogen-rich "sixfold interstices" between tri-s-triazine units give the carrier unique potential to stabilize various metal species (i.e., as single atoms, dimers, trimers, clusters, or nanoparticles).[5a,8,9,13]

This poses the fundamental question: how versatile is g-C₃N₄ as a single-atom host for different metals? To investigate this, here we compare the introduction of five catalytic metals (Pd, Ag, Ir, Pt, and Au) into g-C₃N₄ of distinct morphology (BCN, MCN, and ECN) by direct and postsynthetic routes (**Figure 1**). The carriers and the resulting SAHCs are characterized in depth to elucidate the structure and porosity of the supports as well as the amount, speciation, oxidation state, and distribution of the metal incorporated. In particular, aberration-corrected scanning transmission electron microscopy (AC-STEM) is extensively applied to assess the single-atom dispersion and stability. DFT calculations and kinetic Monte Carlo (KMC) simulations are conducted to gain insight into the adsorption and diffusion of the metals within the carriers. Finally, evaluation in the semi-hydrogenation of 1-hexyne demonstrates the impact of the synthesis method and carrier morphology on the performance of selected SAHCs.

2. Results and Discussion

2.1. Carrier Properties

Bulk, mesoporous and exfoliated g-C₃N₄ carriers were prepared to examine the impact of the carrier morphology on the metal stabilization. BCN was obtained by the direct polymerization of dicyandiamide, MCN was synthesized by a similar approach exploiting colloidal silica as a template and ECN was derived by the thermal delamination of BCN. The significantly enhanced surface area of MCN and ECN with respect to BCN was evidenced by argon sorption (Figure S1, Supporting Information), which also revealed a narrower pore size distribution in MCN compared to ECN. Compared to BCN, which is virtually nonporous, MCN and ECN exhibit significantly higher uptakes over the whole range of relative pressures, reflecting their enhanced mesopore surface area (165 and 245 vs 7 m² g⁻¹, respectively) and associated pore volumes (Table S1, Supporting Information). A prominent hysteresis loop, typical of connected spherical or cylinder mesopores, is observed at $p/p_0 = 0.5$–0.9 for MCN, whereas ECN displays only minor hysteresis, consistent with the presence of nonuniform slit shaped pores between the layered sheets. As seen in the corresponding mesopore size distributions (Figure S1 in the Supporting Information, inset), MCN displays a pronounced peak centered around 15 nm, whereas ECN shows a broad distribution from 3 to 30 nm.

The distinct morphologies of the resulting samples are visible in bright field (BF) transmission electron microscopy (TEM) images (**Figure 2**). Consistent with the expected
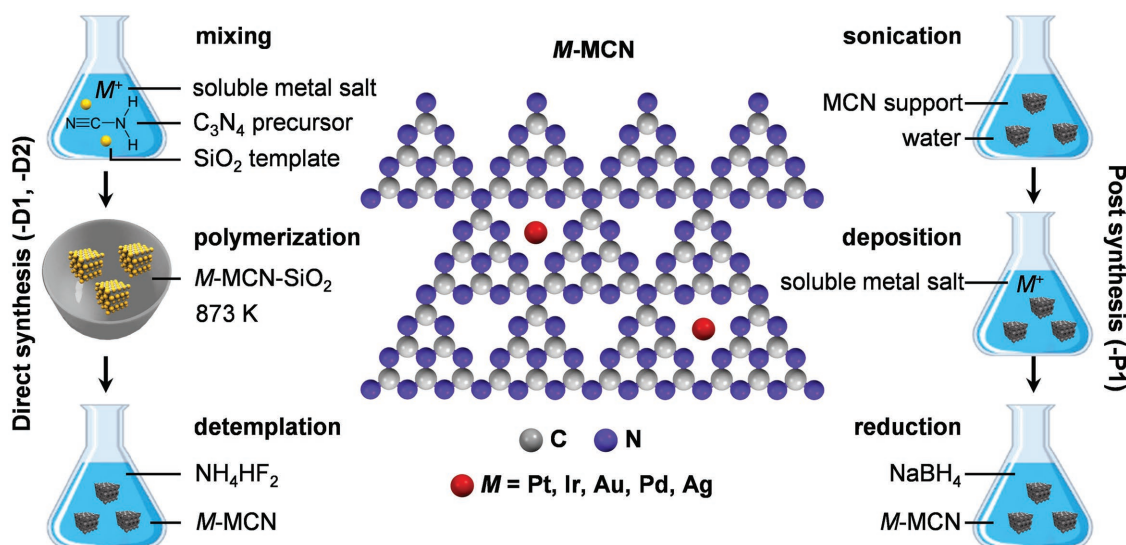

Figure 1. Direct synthesis (−D1, −D2) and postsynthesis (−P1) approaches to stabilize metal atoms within g-C₃N₄, exemplified for the mesoporous MCN carrier. In the idealized location depicted, the metal atom is coordinated by up to six nitrogen atoms within interstices defined by the packing of the tri-s-triazine units.
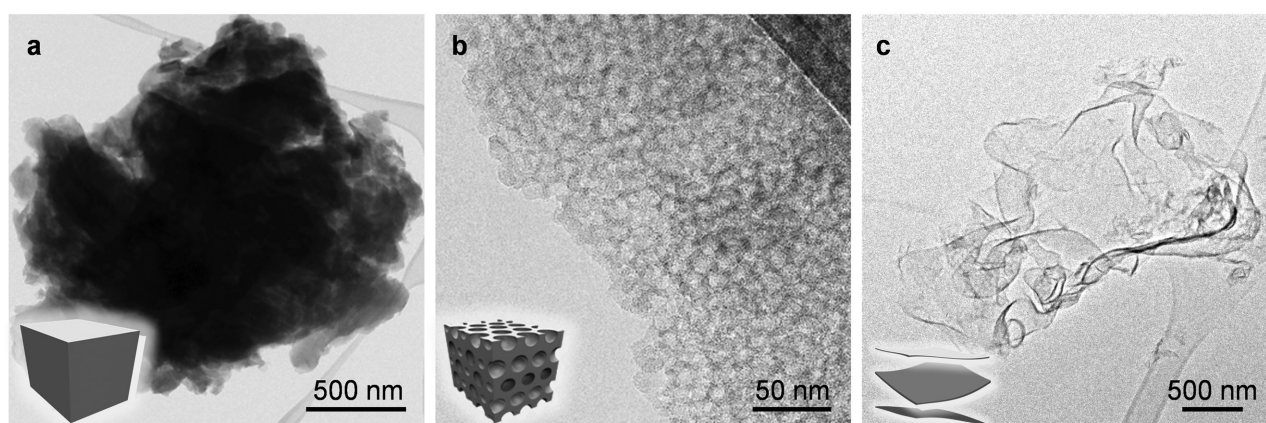
Figure 2. Bright field TEM images of the a) BCN, b) MCN, and c) ECN carriers. The schematics inset illustrate structural models.

densification during the synthesis, BCN (Figure 2a) is comprised of large irregularly shaped particles. In contrast, MCN (Figure 2b) exhibits numerous spherical mesopores with a diameter of ≈12 nm, reflecting the size and geometry of the colloidal silica template. Comparatively, ECN (Figure 2c) displays smaller less dense particles of rumpled sheet-like morphology. These observations are supported by additional high-angle annular dark field (HAADF) STEM images, while the observation of a clear diffraction ring characteristic of graphite-like interlayer stacking confirms the partially crystalline nature in all cases (Figure S2, Supporting Information). Additional diffraction rings can also be seen, but are significantly weaker and more diffuse, characteristic of in-plane structural disorder.

X-ray diffraction (XRD) patterns confirm the similar crystalline structure in all the carriers (Figure S3, Supporting Information). The reflections at 13.1° (100) and 27.3° (002) 2θ stem from the in-plane repeating motifs and graphite-like interlayer stacking, respectively.[11a] However, the lower intensity of the most prominent reflection at 27.3° 2θ observed for MCN and ECN indicates that the introduction of mesoporosity was accompanied by an increased disorder in the g-C_3N_4 layer stacking. Furthermore, a shift of the (002) reflection from 27.3° to 28.0° 2θ, reveals a slight reduction in the interlayer distance (from 0.33 to 0.32 nm) in ECN, which can be attributed to a planarization of the g-C_3N_4 layers during the thermal oxidation etching process.[14] ^{13}C solid-state cross polarization/magic angle spinning nuclear magnetic resonance (CP/MAS NMR) spectroscopy further demonstrate the similarity of the chemical structures. The two main signals at 164 and 157 ppm are attributed to $CN_2(NH_x)$ and CN_3 moieties, respectively.[15]

The molar C:N ratios determined by elemental analysis (around 0.66; Table S1, Supporting Information) are similar to the formula of the "melon" form of graphitic carbon nitride form reported by Lotsch et al.[15] Note that some variation from the ideal formula "C_3N_4" can be expected due to the relatively low crystallinity of the samples investigated, though for simplicity we still refer generally to "g-C_3N_4". In fact, hydrogen contents varying from 1.1 to 2.0 wt% have been reported depending on the synthesis protocol.[16] In comparison to BCN, the increased hydrogen and oxygen content in ECN are due to more exposed NH_x groups and to the oxidation of g-C_3N_4

during the thermal etching process. Similarly, higher defect concentrations in the case of MCN result from the presence of the template, which can disrupt the polymerization process and requires further aqueous workup steps for its removal.

The atomic structure of the carriers was further investigated by X-ray photoelectron spectroscopy (XPS) in Figure S3 in the Supporting Information. A single broad contribution in the C 1s spectra at 288.3 eV, corresponds to the CN_3 bonds in the tri-s-triazine rings. Comparatively, the N 1s spectra can be deconvoluted into three main peaks at 398.7 eV (ring nitrogen, C−N=C), 399.8 eV (tertiary nitrogen, NC_3), and 400.9 eV (NH_x groups). The observation of tertiary nitrogen groups and the C−N=C/NC_3 ratio of around 6 in all the carriers, are fully consistent with a structure based on tri-s-triazine as the main repeating unit.[17] Compared to BCN, the slightly higher NH_x/NC_3 ratio (1.6 vs 1.7) for ECN together with the higher hydrogen content evidenced by elemental analysis, point toward the exposure of more surface NH_x groups upon thermal exfoliation. The slightly lower ratio of 1.5 for MCN can be attributed to the partial substitution of surface NH_x groups with oxygen-containing groups, in agreement with the higher oxygen content of this sample.

Additionally, thermogravimetric analysis (TGA) profiles evidence a slightly decreased thermal stability for MCN (Figure S3, Supporting Information), confirming the reduced structural order in this sample. In general, all the g-C_3N_4 carriers exhibit high thermal stability up to 773 K, making them very promising carriers for single-atom catalysis. Analysis by diffuse reflectance infrared Fourier transform spectroscopy (DRIFTS, Figure S3 in the Supporting Information) confirms the existence of condensed aromatic CN heterocycles.[15] The band at 816 cm^{-1} coincides with the deformation vibrations of the tri-s-triazine ring, while those at 1278, 1343, and 1502 cm^{-1} are attributed to the aromatic C−N heterocyclic stretching and those at 1594 and 1718 cm^{-1} to C=N stretching. The broad bands between 3000 and 3300 cm^{-1} are related to the uncondensed terminal NH_x stretching. Another band at 2173 cm^{-1} in MCN (and weakly present in ECN and BCN) can be assigned to poorly-polymerized cyano groups (C≡N) or cumulated double bonds (N=C=N).[18] Nonetheless, MCN and ECN exhibit more structural defects than BCN (for example exposed NH_x and oxygen-containing groups or poorly polymerized cyano groups),

which could impact the effective stabilization of metal centers in these carriers.

2.2. Metal Stabilization

To study the versatility of g-C$_3$N$_4$ as a single-atom host, five metals (Pd, Ag, Ir, Pt, and Au) were introduced into the carriers by direct and postsynthetic routes, targeting a metal loading of 0.5 wt%. Herein, a distinction in direct approaches is made between the use of inorganic metal salts (coded-D1) and organic metal salts containing a group that can be copolymerized with the applied g-C$_3$N$_4$ precursors (coded-D2). Alternatively, the metals were introduced by the postsynthetic wet deposition coupled with a separate reduction step (coded-P1), see Figure 1. The latter method enabled the highest control over the metal content, which was close to the targeted amount in all cases. Comparatively, larger deviations in the metal loading were observed for samples prepared by direct methods due to the reduced control over the polymer yield (Table S2, Supporting Information). The absence of reflections associated with metal phases in the XRD patterns suggests a high dispersion, except in the case of Au-MCN-D2 for which reflections corresponding to the metal phase were clearly identified, where the peaks indicated by the arrows at 38.2° and 44.4° 2θ are assigned to the (111) and (220) lattice planes, respectively (Figure S4, Supporting Information).

To identify the presence of single metal atoms, dimers, clusters, or nanoparticles, the samples were examined by STEM. The influence of the carrier morphology was studied by comparing the postsynthetic introduction of metals. Isolated metal atoms were observed in all of the catalysts, but coexisted with nanoparticles in some cases as summarized in Table S2 in the Supporting Information. For example, Pt nanoparticles were observed in all samples prepared by wet deposition, and the size and amount varied with the carrier morphology (**Figure 3**a–c). Specifically, Pt-BCN-P1 exhibited a high number of large aggregated nanoparticles up to ≈20 nm in diameter, whereas smaller nanoparticles (≈1 nm in diameter) were observed in Pt-ECN-P1 and Pt-MCN-P1 and were less prevalent in the latter sample. In comparison, the postsynthesis method led to a much better metal dispersion in the case of Pd and Ir (Figures S5 and S6, Supporting Information). Exceptionally, no nanoparticles were found in Ir-MCN-P1 and very few nanoparticles were found in Ir-ECN-P1 or Ir-BCN-P1. The increased formation of nanoparticles in the case of BCN is unsurprising given the low surface area and dense nature of this carrier. The enhanced metal incorporation observed for MCN with respect to ECN possibly relates to the higher defect concentration evidenced in the former carrier, as apart from the coordination sites in the lattice, structural defects are also believed to promote the anchoring of single atoms.[19]

Due to the higher dispersion achieved upon increasing the mesoporosity of the sample, the impact of the synthesis approach was studied on this carrier. Unlike the postsynthetic protocol, atomic dispersions were attained for Pt via direct approaches, as highlighted for Pt-MCN-D1 (Figure 3d) where the high atomic number metal atoms are readily visible as bright dots on the low atomic number MCN support. In fact, the copolymerization approach uniquely enabled the
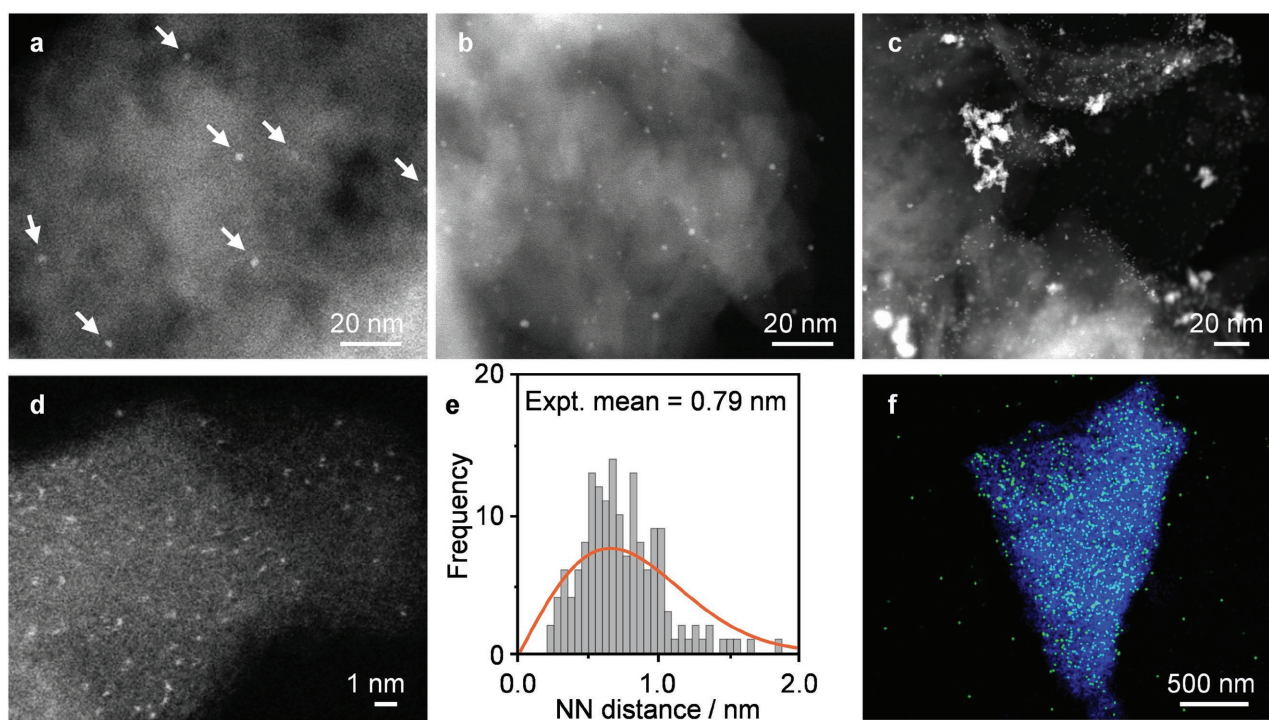

Figure 3. STEM HAADF images of a) Pt-MCN-P1, b) Pt-ECN-P1, c) Pt-BCN-P1, and d) Pt-MCN-D1, e) corresponding nearest neighbor (NN) distances of the Pt atoms in Pt-MCN-D1, compared to those expected for a random distribution of points in the same area (red line), and f) EDXS elemental map of N (blue) and Pt (green) for Pt-MCN-D1. The arrows in (a) indicate nanoparticles, which are also clearly seen in (b) and (c).

introduction of up to 1.4 wt% single Pt atoms on g-C_3N_4, which is one of the highest metal loadings reported with single-atom dispersion to date.[20] Similarly, high dispersions were attained for the Pd- and Ag-containing samples (Figure S7, Supporting Information), although a few nanoparticles were observed in Pd-MCN-D1. This is consistent with earlier findings[8] that no nanoparticles were observed even when 6 wt% Ag was incorporated into g-C_3N_4 by copolymerization. Thus, copolymerization appears to be the most efficient strategy to achieve a high metal loading with 100% single-atom dispersion, while wet deposition leads to the highest tendency of nanoparticle formation. AC-STEM HAADF images, with atomic number contrast, revealed that single Pd, Ag, Ir, and Pt atoms were well dispersed across the MCN samples, as shown in Figures S5, S7, and S8 in the Supporting Information.

The dispersion of the atoms may be characterized through quantitative analysis of the atom positions. A histogram of the nearest neighbor (NN) distances measured for Pt-MCN-D1 is shown in Figure 3e. The corresponding red curve is the calculated NN distance distribution assuming a random dispersion of atoms on the support surface and using the measured metal atom areal density. The good match between the experimental NN distance histograms and the calculated Rayleigh distributions[21] indicates that the atoms are generally dispersed in a random fashion, with little evidence for significant clustering. Similar curves are seen for the other systems studied carrier in Figure S9 in the Supporting Information. While regions of well-dispersed single atoms were identified in all of the samples, AC-STEM HAADF imaging evidenced some metal dimers with atom–atom spacings ($\approx$0.25 nm) significantly smaller than the mean NN distance (Figure S9, Supporting Information). Although this is not definitive proof of dimerization, it is highly suggestive of dimer presence. In the AC-STEM HAADF images from Pt-MCN-P1 and Pd-MCN-P1, as well as well-dispersed single Pt and Pd atoms, crystalline nanoparticles (2–5 nm in size) were found in addition to sub-nm atom clusters (see Figure S8 in the Supporting Information). Although the current density used was kept relatively low, there is no doubt that the energy imparted by the 300 kV electron beam to the individual metal atom species ($\approx$4 eV) may be sufficient to displace some of the metal atoms whilst imaging. This can lead to image artefacts (metal atom "streaking") and to recording atoms twice, or not at all, when displaced from their point of origin to a new site. In addition, the 3D structure of the supports means that two well-separated metal atoms at different heights may appear very close in projection. The relatively low atomic number of g-C_3N_4 means that it is likely to undergo some beam damage and possible atom rearrangement. Confirmation of the uniform distribution of the metal over the MCN carrier was obtained by energy-dispersive X-ray spectroscopy (EDXS) mapping (Figure 3f; Figure S10, Supporting Information). Note the clear observation of the Pt nanoparticles in Pt-MCN-P1 around the edges of the support.

To further investigate the isolation of metal atoms in g-C_3N_4, a model sample (Ir-ECN-P2) was prepared by simultaneous solvent-assisted reduction in ethylene glycol and analyzed using a dedicated aberration-corrected "gentle" STEM. This allowed a more detailed assessment of the metal atom location and the underlying ECN support. A number of single Ir atoms can be
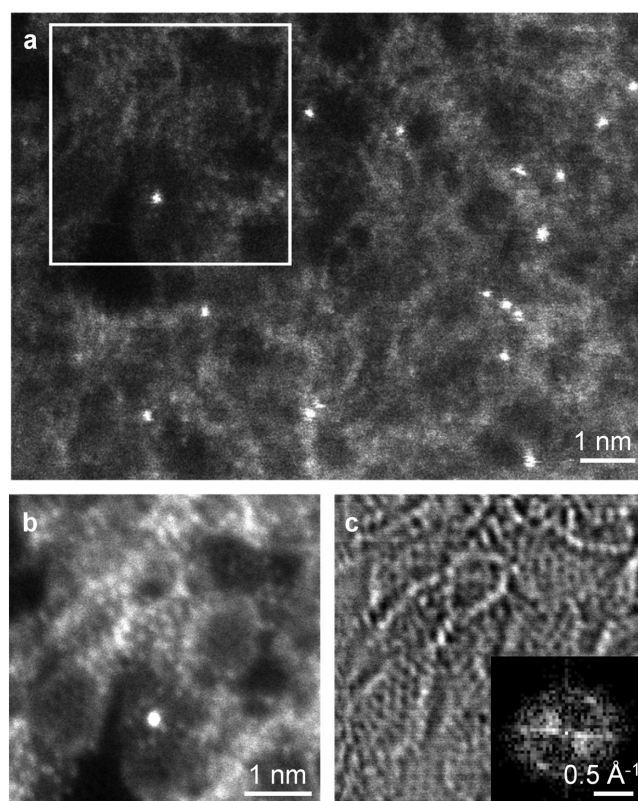

Figure 4. "Gentle STEM" analysis of a model Ir SAHC. a) Atomically resolved STEM HAADF image showing Ir atoms distributed across the ECN support, b) simultaneous STEM HAADF, and c) BF images of the boxed region in (a). The inset in (c) is a local Fourier transform taken from the lower left hand region of the image. These images are a sum of 50 frames acquired rapidly over $\approx$50 s and summed to produce images with high contrast and clarity. The very bright dot in (b) is a single Ir atom anchored on a g-C_3N_4 raft.

observed (**Figure 4**a), the low metal loading (0.02 wt%) ensuring the relative isolation of the atoms. Analysis at higher magnification (Figure 4b) evidences rafts of dots of triangular nature that are reminiscent of the 3×3 triangular arrays expected from the idealized packing of tri-s-triazine. The bright-field (BF) image (Figure 4c) shows the same arrangement of atoms, but the phase contrast reveals more dramatically the underlying structural complexity of the ECN carrier. A Fourier transform of the BF image confirms the local crystalline order.

Further insight into the interaction of the metal species with the g-C_3N_4 carriers was obtained by XPS. Comparison of the XPS spectra of Pt-MCN (**Figure 5**a), Ir-MCN (Figure 5b), and Pd-MCN (Figure 5c) samples reveals a clear impact of the synthesis route, with direct approaches leading to the largest shifts to higher binding energies than that of the corresponding metal in all cases. For example, the Pt $4f_{7/2}$ peaks located at 73.6 eV evidence the presence of cationic $Pt^{\delta+}$ ($2 < \delta < 4$) in Pt-MCN-D1.[22] On the other hand, the Pt $4f_{7/2}$ peaks centered at 70.6 and 72.8 eV in Pt-MCN-P1, indicate a mixed valence state of Pt^0 and Pt^{2+}. This finding agrees with the microscopy observations of both single atoms and nanoparticles in the latter sample. Comparatively, Ir^{4+} species (Ir $4f_{7/2}$ peak at 63.2 eV) are identified in Ir-MCN-D1, while Ir-MCN-P1 displays a single Ir
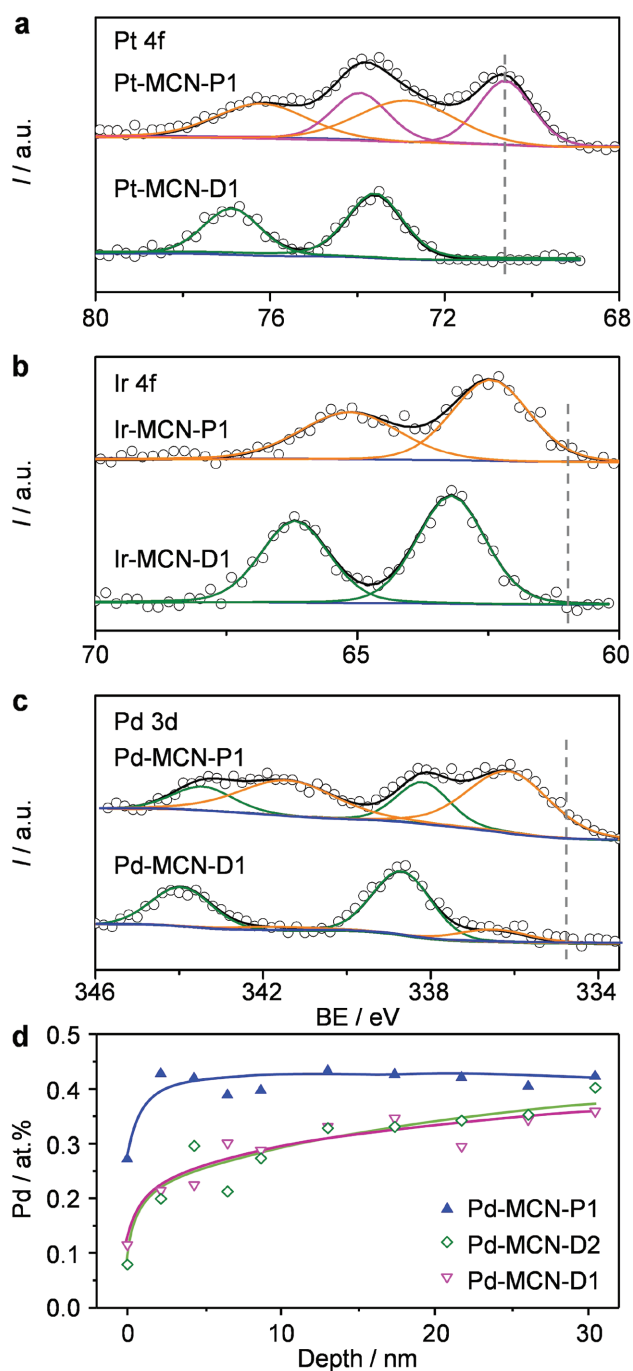
Figure 5. Comparison of the a) Pt 4f; b) Ir 4f; c) Pd 3f core level XPS spectra. The black lines show the result of fitting the raw data (black symbols), whereas the lines corresponding to the individual peaks are colored according to the strength of the metal–carrier interaction, varying from green (strongest) to orange to pink (weakest). The blue lines indicate the background applied. The gray dashed lines in (a–c) indicate the position of metallic species; d) the XPS depth profile analysis of Pd 3d via Ar sputtering at various depths (0–30 nm).

$4f_{7/2}$ peak at 62.5 eV, which is also much higher than that of metallic Ir (60.9 eV).[23] This confirms that Ir species introduced postsynthetically are reduced to a certain degree upon treatment with $NaBH_4$ and partially coordinated to N in the g-C_3N_4

network. Similarly, Pd-MCN-D1 exhibits a higher proportion of Pd^{4+} (338.7 eV) than Pd-MCN-P1 and no metallic Pd (334.9 eV) was evidenced in either sample.

These results demonstrate the strong interaction of the metal species with the N atoms in the carrier. The cationic nature of Pt and Pd upon isolation in g-C_3N_4 agrees with the calculated Bader charges (Table S3, Supporting Information) and the DFT calculated shifts for Pt (ΔBE = 0.82 eV, Table S4 in the Supporting Information). DFT simulations hint that isolated atoms on surface, subsurface positions, and with adsorbed hydrogen might be responsible for the peak observed at low binding energies (70.6 eV) in the $4f_{7/2}$ XPS spectra of Pt-MCN-P1. Previous studies for atoms on highly oriented pyrolytic graphite suggested that the isolated atom value is around 68 eV (shift of −2 eV with respect to Pt(111)),[24] our calculated shift is ΔBE = −1.2 eV for isolated atoms. Although the bathochromic shift of the binding energy could also reflect the formation of small nanoparticles, based on the abundant presence of single atoms evidenced by microscopy this should not have a significant contribution.[24]

2.3. Density Functional Theory and Kinetic Monte Carlo Simulations

DFT and KMC simulations were undertaken to gain further understanding into the energetics of adsorption and diffusion of different metals on g-C_3N_4. Here, this is exemplified for Pd and Pt representing two extreme cases. DFT calculations identified four metastable positions of isolated metal atoms (denoted as s, u, v, and w, respectively) above and below the interstices between the tri-s-triazine units in the top layers of g-C_3N_4 (**Figure 6**a). In the simulations, metal atoms could move between these positions following the paths shown in Figure 6b. Metal atoms could also diffuse between neighboring s positions on the external surface. Additionally, similar paths are expected deeper in the material, so the findings are also relevant for bulk g-C_3N_4 layers. According to the calculated energy profiles, Pt_{2u} dimers and Pd atoms in u positions are expected to be most stable in g-C_3N_4. Figure 6c shows the corresponding energy profiles for the translocation of Pt and Pd atoms along these paths. In the case of Pt, the lower barriers for diffusion from u → v and v → w than for the reverse paths favor the sorption of metal atoms into the bulk. Contrarily, Pd atoms preferentially locate close to the surface in u positions.

DFT calculations further reveal two stable positions of metal dimers, shown in Figure 6d,e. In the first case, one atom sits in an s site and the other is externally bonded to it. Such dimers (denoted Pt_{2s} or Pd_{2s}) form by association of pairs of metal atoms from neighboring s positions. Dimers of the second type (denoted Pt_{2u} or Pd_{2u}) are located deeper in the surface layer and form by association of pairs of atoms from neighboring u and v positions. Note a visible reorganization of nearby C and N atoms around such subsurface dimers. The DFT-calculated energy profiles in Figure 6f summarize the association and decomposition of metal dimers. In the case of Pt, the formation of dimers of both types is favorable and for Pt_{2u} it occurs without any visible energy barrier. However, considering that the diffusion energies of Pt atoms do not favor their presence
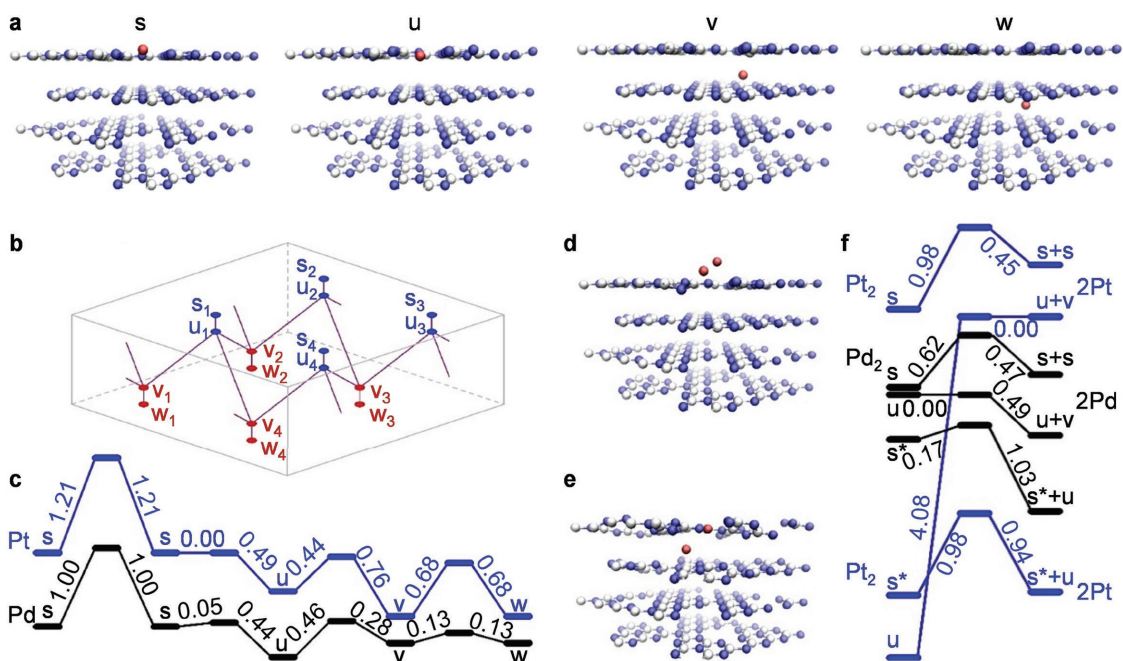
Figure 6. a) DFT optimized incorporation of metal atoms in g-C₃N₄ (M = red, C = white, N = blue), showing the four identified equilibrium positions of metal atoms. Two are located slightly above (s) and below (u) the sixfold cavities between the tri-s-triazine units in the surface g-C₃N₄ layer, and another two are found above (v) and below (w) the sixfold cavities in the subsurface g-C₃N₄ layer. Some C and N atoms have been hidden to facilitate visualization of the metal. b) Identified transition paths of metal atoms inside the surface and subsurface layers of g-C₃N₄. c) Corresponding energy profiles for translocation of Pt and Pd atoms along these paths. d,e) Identified equilibrium positions of metal dimers above (d) and below (e) the surface layer of g-C₃N₄. f) Energy profiles for the association of metal dimers and their decomposition into pairs of atoms located in neighboring s + s, s* + u, or u + v positions (s* denotes s-sites occupied by hydrogenated, thus, immobile metal atoms or dimers).

in s positions, only Pt_{2u} dimers are expected. In the case of Pd, only Pd_{2s} dimers are stable, as Pd_{2u} dissociate into pairs of atoms in u and v positions without any significant energy barrier. However, due to the small energy barrier for the translocation of Pd atoms from s to u positions, the formation of Pd_{2s} is unlikely.

To support these conclusions, KMC simulations were undertaken with the model including the described pathways for metal diffusion, association, and dimer decomposition (**Figure 7**a–d), identifying the variation in the fraction of different isolated atoms and dimers as a function of time. In the case of platinum, all metal atoms move almost instantly into u positions from s positions, irrespective of their initial positions. From there they start to associate into Pt_{2u} dimers and the kinetic curves demonstrate that this process occurs simultaneously to the translocation of metal atoms from u to v positions, necessary to access the $Pt_u + Pt_v \rightarrow Pt_{2u}$ association path. Most Pt atoms associate into dimers within 1 s, while a small fraction remain in positions v and w. As the model does not consider any further translocation of atoms below w positions, all the atoms eventually associate into dimers. In reality, some atoms would be expected to adsorb deeper into the bulk of the carrier. In the case of Pd, no dimer formation is predicted. All metal atoms move from s to u positions almost instantly, where they remain. After around 1 s some atoms also move into subsurface u and v positions.

To investigate the role of the carrier morphology, the initial metal concentration was varied to reflect the relative surface concentrations expected due to the difference in surface area

(almost 20-fold) between the carriers (Figures S11 and S12, Supporting Information). In agreement with experimental observations, the results confirm that increased local surface concentrations would promote dimer formation and thus the stabilization of single atoms would be preferred in mesoporous materials with high surface areas as ECN or MCN. The varying capacity of different metal atoms to form dimers is an important design tool, since this will precede the formation of nanoparticles. However, the processes leading to the formation of the latter are difficult to introduce in the simulations.[25]

Potential differences in the direct and postsynthetic methodologies were also analyzed by varying the initial metal distributions in the simulations, placing the atoms all over the material (Figure 7b,d) or at one surface (Figure 7a,c), respectively. Significant dimerization was observed for Pt in both cases, while Pd mostly remained as single atoms. However, postsynthetic approaches have drawbacks in the isolation of single atoms as the local surface concentration might be very high, promoting aggregation. Direct methodologies are better suited for this purpose, but the entrapment of the metal within the carrier may decrease the atom efficiency, in agreement with the catalytic tests (vide infra). The metal precursor can also be expected to play an important role as the adhesion of the precursor to the surface might be different as we have illustrated by the adsorption of the different precursors to the voids in the C₃N₄ polymers. Comparison of the adsorption energies of the $PdCl_2$ and H_2PtCl_6 precursors applied in this study reveals significantly different values of 1.28 and 1.85 eV, respectively. The stabilization of single atoms could also be strongly reinforced
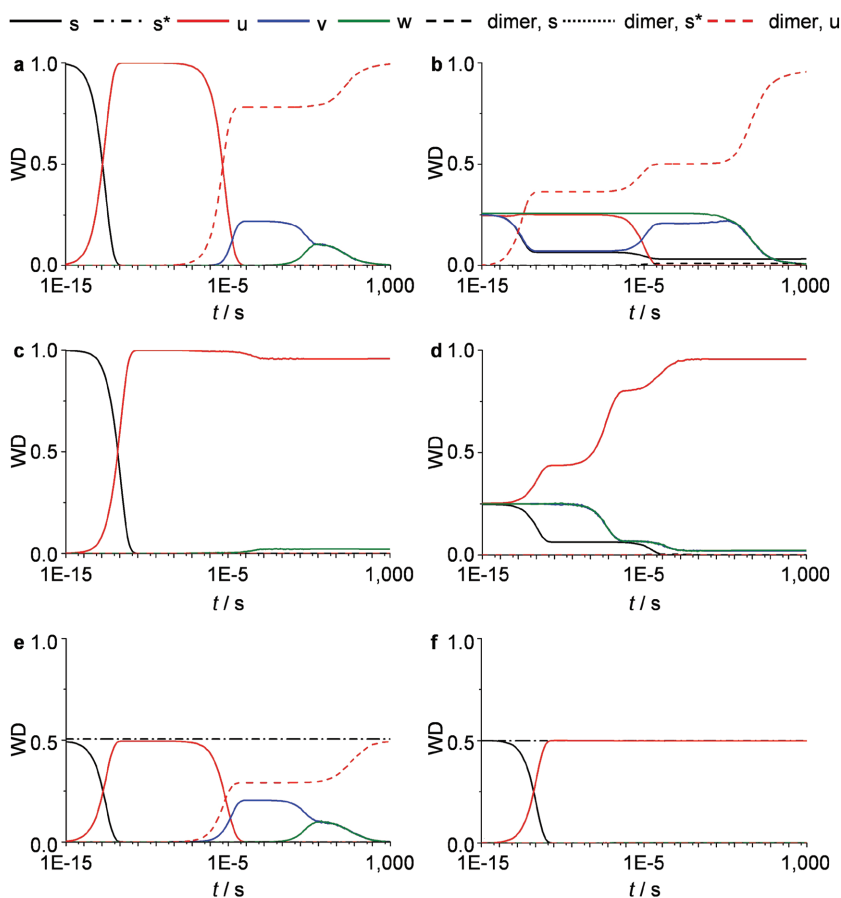
Figure 7. KMC simulations at 300 K comparing the weight distribution of different a,b) Pt and c,d) Pd species with time. In the first simulations a,c), all s sites are occupied by atoms in the initial state, which are free to move during the simulation, other sites are vacant. In the second simulations b,d) the same amount of atoms is initially distributed uniformly between all sites. KMC simulations illustrating the impact of hydrogen on the stabilization of e) Pt and f) Pd atoms in g-C_3N_4. In all cases 50% of the atoms are hydrogenated in the initial state and thus fixed in their positions, while 50% are free to move. The metal distribution in the initial state only occupies the s-sites.

phase and this behavior is retained on g-C_3N_4 as a result of the relatively tunable interaction between the matrix and the metal. Comparatively, the formation of Ir dimers is energetically favorable, but the formation energy of surface and subsurface atoms on g-C_3N_4 is also high. This finding along with the aforementioned propensity for Pt dimerization revealed by DFT and KMC is consistent with the AC-STEM observations, where evidence for dimers is seen in both systems (Figure S5, Supporting Information). Moreover, that the closed-shell nature of the isolated atoms and dimers can affect the reactivity of these materials. Furthermore, the calculated energies suggest that the stability of metal atoms or dimers alone cannot explain the observed experimental behaviors. Other factors such as the synthesis protocol and defect structure likely play a role in the stabilization of single atoms in the g-C_3N_4 compounds, as illustrated by the significant impact observed in the presence of low concentration of hydrogen atoms.

2.4. Catalytic Performance

To study the impact of the synthetic approach on the performance, selected SAHCs were evaluated in the continuous-flow semihydrogenation of 1-hexyne. The catalytic tests focused on the Pd-containing samples as the most efficient metal for this reaction. Interestingly, despite exhibiting a comparable metal content and speciation (Table S2, Supporting Information), Pd-MCN-P1 exhibits a significantly higher activity than Pd-MCN-D1 or Pd-MCN-D2 (**Figure 8**; Figure S15, Supporting Information). For example, at 303 K and 1 bar the reaction rate over Pd-MCN-P1 was four times that of Pd-MCN-D1 and six times that of Pd-MCN-D2. Comparatively, the SAHCs synthesized by direct approaches demonstrated an excellent intrinsic selectivity (around 100%), while the sample prepared by postsynthetic methods were slightly less selective (e.g., 90%–100%) also yielding small amounts of over hydrogenated products (Figure S16, Supporting Information).

Consistent with the findings of the theoretical simulations, the improved activity of Pd-MCN-P1 is tentatively ascribed to the enhanced fraction of accessible metal sites located at the carrier surface endowed by the postsynthetic route in contrast to the more homogeneous 3D dispersion obtained by direct synthesis. This is further supported by depth-profiling the compositional variation by XPS coupled with ion etching (Figure 5d), which revealed a surface Pd content of Pd-MCN-P1 over double that of Pd-MCN-D1 or Pd-MCN-D2. All samples showed an increased concentration upon removal of the surface layers, tending toward 0.4 at%, but this valued was reached at a depth of ≈5 nm in Pt-MCN-P1 compared to ≈30 nm in Pd-MCN-D1

by the reduction of the metal precursors. When the KMC simulations are rerun including one H atom bound to an N atom in g-C_3N_4 and a second H atom connected to the metal atom in the form of a hydride (Figure 7e,f; Figure S13, Supporting Information, while the idealized structure model is shown in Figure S14 in the Supporting Information), the number of dimers decreases considerably for both Pd and Pt. Thus, the preparation of SAHCs based on g-C_3N_4 could be assisted by the reduction agent to yield isolated atoms on the surface. Note that the generation of hydride metal species at the external surface may be promoted by using strong reducing agents as borohydrides. However, high local concentrations of reduced metal atoms may also promote nanoparticle formation.

Finally, the formation energy of different species of all the metals studied is summarized in Table S5 in the Supporting Information. The energies are calculated with respect to isolated metal atoms in the gas phase and on the surface of the carriers and compared to those determined for dimerization (which are close to literature values).[26] In particular, it is notable that Pd and Ag are notably less prone to dimer formation in the gas

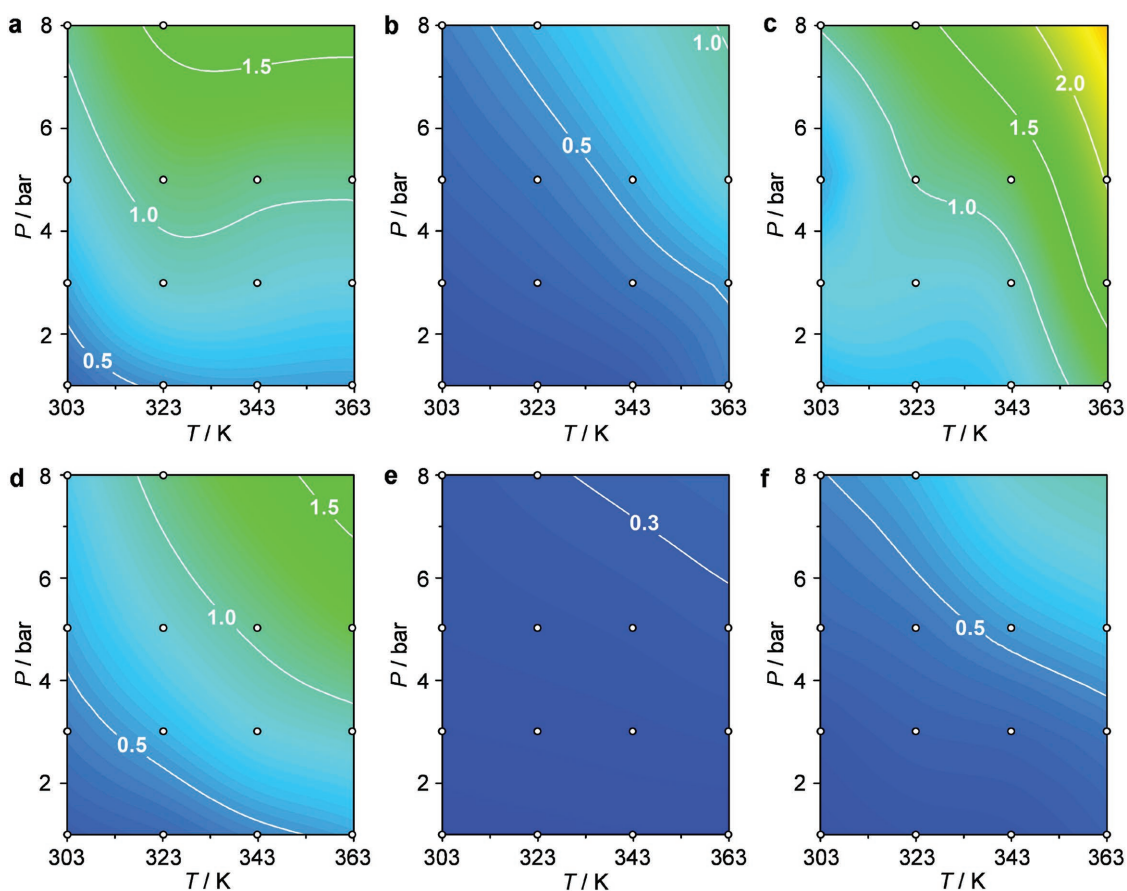**Figure 8.** Reaction rate of 1-hexyne hydrogenation (in 10^3 $mol_{1\text{-hexene}}$ mol_{Pd}^{-1} h^{-1}) at different temperatures and pressures over a) Pd-BCN-P1; b) Pd-MCN-0.5-P1; c) Pd-MCN-P1; d) Pd-BCN-D2; e) Pd-MCN-D1, and f) Pd-MCN-D2. The contour maps were obtained through spline interpolation of 14 experimental points. Reaction conditions: W_{cat} = 0.1 g, F_L (1-hexyne + toluene) = 1 cm^3 min^{-1} and F_G (H_2) = 36 cm^3 min^{-1}.

and Pd-MCN-D. In addition to the reduced accessibility of the metal, the stronger interaction with the carrier in the samples obtained by direct routes could also play a role, the charge transfer making the metal atoms inert.

Considering the effect of the carrier morphology, Pd-BCN-P1 and Pd-BCN-D2 exhibit comparable activity to Pd-MCN-P1. This is unsurprising since although both samples based on bulk g-C₃N₄ display very low surface areas, the microscopy observations (vide supra) demonstrated the presence of abundant Pd nanoparticles, which likely originate the activity of these catalysts. Nonetheless, a superior selectivity is still observed over Pd-BCN-D2 with respect to Pd-BCN-P1, indicating subtle differences in the metal speciation between the samples which are difficult to quantify based on visualization alone. As an additional reference, a mesoporous carrier with roughly half the surface area (S_{BET} = 125 m^2 g^{-1}) was synthesized and Pd was introduced postsynthetically (coded Pd-MCN-0.5-P1). Interestingly, despite presenting both nanoparticles and single atoms, this sample exhibited reduced activity with respect to both Pd-BCN-P1 and Pd-MCN-P1. These observations suggest a tight interplay between mesopore surface area, nanoparticle formation, and the amount of single atoms accessible on the external surface of the catalysts. Clearly, tailoring the metal dispersion and the strength of the interaction with the carrier pose urgent

challenges in the design of effective SAHCs. In this direction, new strategies to isolate active metal species at the carrier surface while preserving an exceptionally high stability should be pursued. Similarly, the preparation of carriers with tailored, for example N deficient, coordination sites would be of interest.

3. Conclusions

This study examined the impact of the carrier morphology, synthesis method, and metal identity on the versatility of g-C₃N₄ as a carrier in the preparation of SAHCs. The isolation of metal atoms was favored by enhancing the external surface area of the carrier, while defects were also found to play an important role. Direct approaches exploiting copolymerizable metal precursors, attained the widest flexibility in the incorporation of different metals. Comparatively, increased control over the metal content and higher number of accessible active sites were attained by the postsynthetic introduction. This resulted in higher reaction rates in the semihydrogenation of 1-hexyne. Simulations of the adsorption, stabilization, and diffusion of the metals, established the stable location close to the sixfold interstices between tri-s-triazine units composing the g-C₃N₄ layers and confirmed the varied accessibility of the metal sites arising from the

different strategies. The findings provide unique insights for the design of SAHCs based on g-C$_3$N$_4$, paving the way to maximize the atom efficiency in a spectrum of catalytic applications.

4. Experimental Section

Carbon Nitride Synthesis: BCN was synthesized by calcining dicyandiamide (10 g) at 823 K (2.3 K min^{-1} ramp rate) for 4 h under a nitrogen flow (15 cm^3 min^{-1}). To prepare MCN, cyanamide (2.5 g) was added to an aqueous dispersion of SiO$_2$ nanoparticles (6.25 g, 40 wt% solids, 12 nm average diameter) and the mixture was stirred for 6 h at 373 K to completely evaporate the water. The resultant solids were then ground and calcined as described above before removing the SiO$_2$ by treatment with an aqueous solution of NH$_4$HF$_2$ (4 M, 100 cm^3) at 293 K for 48 h. The carrier was collected by filtration, washed thoroughly with distilled water and ethanol and subsequently dried at 323 K under vacuum. ECN was obtained via the thermal exfoliation of BCN (3 g) at 773 K (5 K min^{-1} ramp rate) for 8 h in static air.

Metal Incorporation: Different approaches were studied to incorporate metals (M = Pt, Ir, Au, Pd, and Ag) into the g-C$_3$N$_4$ carriers (Figure 1). Two direct routes employed either a soluble inorganic salt (coded D1, 10.5 mg H$_2$PtCl$_6$·xH$_2$O, 15.4 mg K$_2$IrCl$_6$·6 H$_2$O, or 8.3 mg PdCl$_2$) or an organic salt capable of copolymerizing with cyanamide (coded D2, 17 mg K$_2$Pt(CN)$_4$·xH$_2$O, 11.2 mg KAu(CN)$_2$, 19.3 mg K$_2$Pd(CN)$_4$·xH$_2$O, or 9.2 mg Ag(C$_4$N$_3$)) as metal precursors. The latter were added to cyanamide or to the mixture of cyanamide and colloidal silica in the synthesis of BCN or MCN, respectively. Postsynthetic metal introduction was achieved by a sequential wet deposition–reduction approach (coded P1). The desired carrier (1 g) was dispersed in H$_2$O (100 cm^3) under sonication. Then, the metal precursor (H$_2$PtCl$_6$·xH$_2$O, K$_2$IrCl$_6$·6H$_2$O, or PdCl$_2$, 0.5 wt% metal relative to the carrier) was added and the slurry was stirred in the dark at 293 K for 1 h. Afterward, NaBH$_4$ (1.4 cm^3, 0.5 M) was added dropwise and stirred overnight. Finally, the solids were separated by filtration, washed thoroughly with H$_2$O and ethanol, and dried overnight at 323 K. For the SuperSTEM studies, a variant of this route (coded P2) was applied to obtain Ir-ECN-P2, ensuring a high metal dispersion. ECN (400 mg) was dispersed in ethylene glycol (40 cm^3, pH = 8) under sonication for 1 h. Then K$_2$IrCl$_6$·6H$_2$O (0.36 cm^3, 4.7×10^{-3} M in ethylene glycol) was added and the slurry was agitated for another 0.5 h in the dark. The resulting suspensions were refluxed at 393 K for 2 h. Finally, the products were isolated following the same protocol as P1.

Characterization: Inductively coupled plasma-optical emission spectrometry was conducted using a Horiba Ultra 2 instrument equipped with photomultiplier tube detection. The solids were dissolved in a piranha solution under sonication until the absence of visible solids. Elemental analysis (C, H, N, O) was determined by infrared spectroscopy using a LECO CHN-900 combustion furnace. Argon sorption was measured at 77 K in a Micrometrics 3Flex instrument, after evacuation of the samples at 423 K for 10 h. The surface area and pore size distributions were determined via the Brunauer–Emmett–Teller/Barrett–Joyner–Halenda methods, respectively. XPS was performed in a Physical Electronics Instruments Quantum 2000 spectrometer using monochromatic Al kα radiation generated from an electron beam operated at 15 kV and 32.3 W. The spectra were collected under ultrahigh vacuum conditions (residual pressure = 5×10^{-8} Pa) at a pass energy of 46.95 eV. All spectra were referenced to the C 1s peak of ternary carbon at 288.3 eV. TGA was performed in a Mettler Toledo TGA/DSC 1 Star system. The analysis was performed in air (40 cm^3 min^{-1}), heating the sample from 298 to 1173 K at a rate of 5 K min^{-1}. ^{13}C solid-state CP/MAS NMR spectra were recorded on a Bruker AVANCE III HD NMR spectrometer at a magnetic field of 16.4 T corresponding to a ^{1}H Larmor frequency of 700.13 MHz. A 4 mm double resonance probe head at a spinning speed of 10 kHz was used for all experiments. The ^{13}C spectra were acquired using a cross polarization experiment with a contact time of 2 ms and a recycle delay of 1 s. A total of 64×10^3 scans were summed

for each sample. ^{13}C experiments used high-power ^{1}H decoupling during acquisition using a SPINAL-64 sequence. Powder XRD was performed in a PANalytical X'Pert PRO-MPD diffractometer operated in Bragg–Brentano geometry using Ni-filtered Cu Kα ($\lambda = 0.1541$ nm) radiation. Data were recorded in the range of 5°–60°2θ with an angular step size of 0.05° and a counting time of 2 s per step. DRIFTS was performed using a Bruker Optics Vertex 70 spectrometer equipped with a high-temperature DRIFT cell (Harrick) and a HgCdTe (MCT) detector. Spectra were recorded in the range of 4000–400 cm^{-1} under N$_2$ flow and at room temperature by coaddition of 200 scans with a nominal resolution of 4 cm^{-1}.

Electron Microscopy: Samples for (scanning) transmission electron microscopy ((S)TEM) were prepared by crushing respective BCN, MCN, or ECN powders between optical lens tissue, followed by dusting onto standard copper mesh holey carbon support films (EMresolutions), Quantifoil, or C-flat support grids. Conventional TEM and STEM imaging was performed on FEI Tecnai Osiris and Talos F200X instruments. AC-STEM was performed using three microscopes: an FEI Titan, a NION UltraSTEM 100, and a NION UltraSTEM 100MC "HERMES".[27] The Titan with XFEG electron source and CEOS probe aberration corrector, was operated at 300 kV with an illumination angle of 20.6 mrad and probe current of ≈60 pA. The SuperSTEM instruments were operated at 60 kV with an illumination angle of 30 mrad and probe current of around 40 pA. STEM HAADF images were acquired on all instruments with the inner angle of the detector chosen to minimize any possible Bragg diffraction contrast and maximize overall image signal, and especially atomic number (Z) contrast between single atoms/clusters and the underlying support. As such, an optimum inner angle was found to be between 30 and 50 mrad on the Titan and 86 mrad on the SuperSTEM instruments. Typical per pixel dwell times were ≈10 and 30 μs, respectively, chosen as the best balance to achieve sufficient signal-to-noise for single atom visibility and to minimize atom movement during imaging. STEM HAADF image contrast can be considered as arising from predominantly incoherent scattering and so images formed with this method may be more interpretable than phase-contrast TEM images. This is particularly useful for interpreting images from complex porous structures and for revealing single atoms, such as studied here. Diffraction patterns were recorded with a defocused STEM probe, to form near-parallel illumination and produce spot/ring patterns, akin to more conventional selected area patterns. Elemental maps using EDXS were acquired on the FEI Talos F200X instrument operated at 200 kV and equipped with an FEI SuperX detector.

The degree of atomic dispersion was measured by quantifying the nearest-neighbor distance of each atom and comparing the obtained distribution to that expected for a random dispersion. The STEM HAADF images were initially filtered using a Laplacian-of-Gaussian filter to enhance the atom contrast. Gaussians were best-fitted to the individual atom images and the centers of the Gaussians were used as the atom locations in subsequent analyses. The areal density, λ, was calculated by summing the number of atoms in a region of interest and dividing by the corresponding area. If atoms are randomly distributed on a plane, then the atom locations will be described by a Poisson random field. The probability density functions (PDF) for the distribution of nearest-neighbor distances (r) should then follow a Rayleigh distribution[21]

$$PDF(r) = 2\pi\lambda r \exp(-\pi\lambda r^2) \qquad (1)$$

where the mean value of the distribution is given by $1/2\sqrt{\lambda}$. Comparing the experimental nearest-neighbor distances to the Rayleigh distribution provides a means by which to ascertain the degree of clustering of the atoms with respect to a random scatter of points. In the present case, all samples show a similar distribution to the random case, suggesting no preferential clustering.

Density Functional Theory and KMC Simulations: The Vienna ab initio simulation package[28] was employed to model the metal atom distributions in the g-C$_3$N$_4$ systems, using the Perdew–Burke–Ernzerhof functional.[29] The projector augmented wave method was employed to represent core electrons[30] and the valence was expanded in plane waves

with a cutoff energy of 450 eV. The C_6N_8 (melon) moieties were built in a graphitic form and the optimized interlayer structure is 3.5 Å. Four-layered slabs of the (0001) surface were built with p (2 × 2) supercells (Figure 6a). The incorporation of metal atoms, precursors, and dimers were assessed on one side of the slab. Transition states were located by the climbing image-nudged elastic band algorithm.[31]

KMC simulations were performed using a custom made code.[32] The elementary cell of the employed simulation lattice and possible pathways for the movement and association of metal atoms inside the g-C_3N_4 systems was developed based on the insights (thermodynamics and barriers) for the elementary diffusion and reaction (dimerization) steps obtained by DFT. The rate of each elementary process was approximated as

$$r = \frac{kT}{h} \exp\left(-\frac{\Delta E}{kT}\right) \tag{2}$$

where k, h, and T are the Boltzmann and Planck constants and the system temperature, and ΔE is the corresponding energy barrier predicted by DFT. Simulations were carried out at 300 K with all surface sites occupied by metal atoms in the initial state. The total size of the system in KMC simulations was 50 × 50 elementary cells.

The role of the type of carrier was addressed by varying the metal concentration. The latter was estimated by considering the targeted metal concentration (0.5 wt%), the density of the coordination sites (1/50 Å^2), and the surface area of the catalyst (e.g ., 155 m^2 g^{-1} for MCN). This corresponds to ≈3.5 × 10^{20} anchoring positions per gram of catalyst and a number of metal atoms of 2.8 × 10^{19}, occupying ≈8%–10% of surface positions assuming all the metal is located at the surface. Based on these values, further concentrations, equivalent to 100%, 50%, and 25% coverage, were also investigated. Two initial configurations were considered; a homogeneous 3D distribution of metal atoms that would better mimic direct synthesis protocols, and an inhomogeneous 2D distribution with all of the atoms at the external surface, representing the postsynthetic approach. The role of the precursor was studied by comparing the adsorption of $PdCl_2$ and H_2PtCl_6 using the methods described in the previous study.[33]

Catalyst Testing: The hydrogenation of 1-hexyne (Acros Organics, 98%) was conducted in a continuous-flow flooded-bed microreactor (ThalesNano H-Cube Pro), in which the liquid feed containing the substrate (5 vol%), toluene (Fischer Chemicals, 99.95%), and gaseous hydrogen (generated in situ by Millipore water electrolysis) flows concurrently upward through a fixed bed of catalyst particles (0.1 g in 0.12 g of silicon carbide, 0.2–0.4 mm diameter) in a cylindrical cartridge (3.5 mm internal diameter). The reaction was conducted at various conditions of temperature (303–363 K) and total pressure (1–8 bar) with fixed liquid (1cm^3 min^{-1}) and H_2 (40 cm^3 min^{-1}) flow rates. The products were collected every 15 min after the reaction reached steady state and analyzed offline using a gas chromatograph (HP-6890) equipped with a HP-5 capillary column and a flame ionization detector. The conversion was determined from the amount of reacted substrate divided by the amount of substrate at the reactor inlet. The selectivity to each product was quantified as the amount of the particular product divided by the amount of reacted substrate. The reaction rate was expressed in moles of product per mole of Pd and unit of time.

Supporting Information

Supporting Information is available from the Wiley Online Library or from the author.

Acknowledgements

[1] a) M. Flytzani-Stephanopoulos, *Acc. Chem. Res.* **2014**, *47*, 783; b) G. Kyriakou, M. B. Boucher, A. D. Jewell, E. A. Lewis, T. J. Lawton, A. E. Baber, H. L. Tierney, M. Flytzani-Stephanopoulos, E. C. H. Sykes, *Science* **2012**, *335*, 1209; c) B. Qiao, A. Wang, X. Yang, L. F. Allard, Z. Jiang, Y. Cui, J. Liu, J. Li, T. Zhang, *Nat. Chem.* **2011**, *3*, 634; d) X.-F. Yang, A. Wang, B. Qiao, J. Li, J. Liu, T. Zhang, *Acc. Chem. Res.* **2013**, *46*, 1740; e) L. Liu, U. Diaz, R. Arenal, G. Agostini, P. Concepcion, A. Corma, *Nat. Mater.* **2017**, *16*, 132; f) S. Liang, C. Hao, Y. Shi, *ChemCatChem* **2015**, *7*, 2559; g) J. M. Thomas, *Phys. Chem. Chem. Phys.* **2014**, *16*, 7647.

[2] a) M. Haruta, *Faraday Discuss.* **2011**, *152*, 11; b) M. D. Hughes, Y.-J. Xu, P. Jenkins, P. McMorn, P. Landon, D. I. Enache, A. F. Carley, G. A. Attard, G. J. Hutchings, F. King, E. H. Stitt, P. Johnston, K. Griffin, C. J. Kiely, *Nature* **2005**, *437*, 1132; c) J. A. Anderson, J. Mellor, R. P. K. Wells, *J. Catal.* **2009**, *261*, 208; d) M. Mavrikakis, P. Stoltze, J. K. Nørskov, *Catal. Lett.* **2000**, *64*, 101.

[3] F. R. Lucci, J. Liu, M. D. Marcinkowski, M. Yang, L. F. Allard, M. Flytzani-Stephanopoulos, E. C. H. Sykes, *Nat. Commun.* **2015**, *6*, 8550.

[4] a) S. Sun, G. Zhang, N. Gauquelin, N. Chen, J. Zhou, S. Yang, W. Chen, X. Meng, D. Geng, M. N. Banis, R. Li, S. Ye, S. Knights, G. A. Botton, T.-K. Sham, X. Sun, *Sci. Rep.* **2013**, *3*, 1775; b) Y.-T. Kim, K. Ohshima, K. Higashimine, T. Uruga, M. Takata, H. Suematsu, T. Mitani, *Angew. Chem. Int. Ed.* **2006**, *45*, 407; c) K. Kamiya, R. Kamai, K. Hashimoto, S. Nakanishi, *Nat. Commun.* **2014**, *5*, 5040.

[5] a) G. Vilé, D. Albani, M. Nachtegaal, Z. Chen, D. Dontsova, M. Antonietti, N. López, J. Pérez-Ramírez, *Angew. Chem. Int. Ed.* **2015**, *54*, 11265; b) H. Wei, X. Liu, A. Wang, L. Zhang, B. Qiao, X. Yang, Y. Huang, S. Miao, J. Liu, T. Zhang, *Nat. Commun.* **2014**, *5*, 5634.

[6] F. Besenbacher, I. Chorkendorff, B. S. Clausen, B. Hammer, A. M. Molenbroek, J. K. Nørskov, I. Stensgaard, *Science* **1998**, *279*, 1913.

[7] J. M. Thomas, *Nature* **2015**, *525*, 325.

[8] Z. Chen, S. Pronkin, T.-P. Fellinger, K. Kailasam, G. Vilé, D. Albani, F. Krumeich, R. Leary, J. Barnard, J. M. Thomas, J. Pérez-Ramírez, M. Antonietti, D. Dontsova, *ACS Nano* **2016**, *10*, 3166.

[9] X. Li, W. Bi, L. Zhang, S. Tao, W. Chu, Q. Zhang, Y. Luo, C. Wu, Y. Xie, *Adv. Mater.* **2016**, *28*, 2427.

[10] a) B. Molina, L. E. Sansores, *Mod. Phys. Lett. B* **1999**, *13*, 193; b) A. Y. Liu, M. L. Cohen, *Science* **1989**, *245*, 841.

[11] a) A. Thomas, A. Fischer, F. Goettmann, M. Antonietti, J.-O. Müller, R. Schlögl, J. M. Carlsson, *J. Mater. Chem.* **2008**, *18*, 4893; b) F. Fina, S. K. Callear, G. M. Carins, J. T. S. Irvine, *Chem. Mater.* **2015**, *27*, 2612; c) J. Liu, H. Wang, M. Antonietti, *Chem. Soc. Rev.* **2016**, *45*, 2308; d) X. Wang, K. Maeda, A. Thomas, K. Takanabe, G. Xin, J. M. Carlsson, K. Domen, M. Antonietti, *Nat. Mater.* **2009**, *8*, 76; e) Z. P. Chen, M. Antonietti, D. Dontsova, *Chem. Eur. J.* **2015**, *21*, 10805.

[12] E. Kroke, M. Schwarz, E. Horath-Bordon, P. Kroll, B. Noll, A. D. Norman, *New J. Chem.* **2002**, *26*, 508.

[13] X.-H. Li, M. Antonietti, *Chem. Soc. Rev.* **2013**, *42*, 6593.

[14] P. Niu, L. Zhang, G. Liu, H.-M. Cheng, *Adv. Funct. Mater.* **2012**, *22*, 4763.

[15] B. V. Lotsch, M. Döblinger, J. Sehnert, L. Seyfarth, J. Senker, O. Oeckler, W. Schnick, *Chem. Eur. J.* **2007**, *13*, 4969.

[16] E. C. Franklin, *J. Am. Chem. Soc.* **1922**, *44*, 486.

[17] C. Fettkenhauer, G. Clavel, K. Kailasam, M. Antonietti, D. Dontsova, *Green Chem.* **2015**, *17*, 3350.

[18] a) V. N. Khabashesku, J. L. Zimmerman, J. L. Margrave, *Chem. Mater.* **2000**, *12*, 3264; b) E. G. Gillan, *Chem. Mater.* **2000**, *12*, 3906; c) M. J. Bojdys, J.-O. Müller, M. Antonietti, A. Thomas, *Chem. Eur. J.* **2008**, *14*, 8177.

[19] a) E. Wahlström, N. Lopez, R. Schaub, P. Thostrup, A. Rønnau, C. Africh, E. Lægsgaard, J. K. Nørskov, F. Besenbacher, *Phys. Rev. Lett.* **2003**, *90*, 026101; b) S. Stolbov, M. Alcántara Ortigoza, *J. Chem. Phys.* **2015**, *142*, 154703; c) I. N. Remediakis, N. Lopez, J. K. Nørskov, *Angew. Chem. Int. Ed.* **2005**, *44*, 1824; d) F. Li, Y. Li, X. C. Zeng, Z. Chen, *ACS Catal.* **2015**, *5*, 544; e) B. L. He, J. S. Shen, Z. X. Tian, *Phys. Chem. Chem. Phys.* **2016**, *18*, 24261.

[20] a) P. Liu, Y. Zhao, R. Qin, S. Mo, G. Chen, L. Gu, D. M. Chevrier, P. Zhang, Q. Guo, D. Zang, B. Wu, G. Fu, N. Zheng, *Science* **2016**, *352*, 797; b) J. Deng, H. Li, J. Xiao, Y. Tu, D. Deng, H. Yang, H. Tian, J. Li, P. Ren, X. Bao, *Energy Environ. Sci.* **2015**, *8*, 1594; c) J. D. Kistler, N. Chotigkrai, P. Xu, B. Enderle, P. Praserthdam, C.-Y. Chen, N. D. Browning, B. C. Gates, *Angew. Chem. Int. Ed.*

[21] M. Utlaut, *Phys. Rev. B* **1980**, *22*, 4650.

[22] a) K. Ding, A. Gulec, A. M. Johnson, N. M. Schweitzer, G. D. Stucky, L. D. Marks, P. C. Stair, *Science* **2015**, *350*, 189; b) M. Yang, J. Liu, S. Lee, B. Zugic, J. Huang, L. F. Allard, M. Flytzani-Stephanopoulos, *J. Am. Chem. Soc.* **2015**, *137*, 3470.

[23] T. W. Hanks, R. A. Ekeland, K. Emerson, R. D. Larsen, P. W. Jennings, *Organometallics* **1987**, *6*, 28.

[24] Y. Sun, Y. Wang, J. S. Pan, L.-I. Wang, C. Q. Sun, *J. Phys. Chem. C* **2009**, *113*, 14696.

[25] R. Addou, T. P. Senftle, N. O'Connor, M. J. Janik, A. C. T. van Duin, M. Batzill, *ACS Nano* **2014**, *8*, 6321.

[26] J. Du, X. Sun, H. Wang, *Int. J. Quantum Chem.* **2008**, *108*, 1505.

[27] a) O. L. Krivanek, T. C. Lovejoy, N. Dellby, R. W. Carpenter, *Microscopy* **2013**, *62*, 3; b) O. L. Krivanek, G. J. Corbin, N. Dellby, B. F. Elston, R. J. Keyse, M. F. Murfitt, C. S. Own, Z. S. Szilagyi, J. W. Woodruff, *Ultramicroscopy* **2008**, *108*, 179; c) O. L. Krivanek, N. Dellby, M. F. Murfitt, M. F. Chisholm, T. J. Pennycook, K. Suenaga, V. Nicolosi, *Ultramicroscopy* **2010**, *110*, 935.

[28] G. Kresse, J. Furthmüller, *Comput. Mater. Sci.* **1996**, *6*, 15.

[29] J. P. Perdew, K. Burke, M. Ernzerhof, *Phys. Rev. Lett.* **1996**, *77*, 3865.

[30] a) P. E. Blöchl, *Phys. Rev. B* **1994**, *50*, 17953; b) G. Kresse, D. Joubert, *Phys. Rev. B* **1999**, *59*, 1758.

[31] G. Henkelman, H. Jónsson, *J. Chem. Phys.* **2000**, *113*, 9978.

[32] S. Pogodin, N. López, *ACS Catal.* **2014**, *4*, 2328.

[33] J. Jover, M. García-Ratés, N. López, *ACS Catal.* **2016**, *6*, 4135.

2014, *53*, 8904; d) J. H. Kwak, J. Hu, D. Mei, C.-W. Yi, D. H. Kim, C. H. F. Peden, L. F. Allard, J. Szanyi, *Science* **2009**, *325*, 1670.